In vivo optical coherence tomography of stimulus-evoked intrinsic optical signals in mouse retinas

Benquan Wang
Yiming Lu
Xincheng Yao

In vivo optical coherence tomography of stimulus-evoked intrinsic optical signals in mouse retinas

Benquan Wang,[a] Yiming Lu,[a] and Xincheng Yao[a,b,*]
[a]University of Illinois at Chicago, Department of Bioengineering, 851 South Morgan Street, Chicago, Illinois 60607, United States
[b]University of Illinois at Chicago, Department of Ophthalmology and Visual Sciences, 1855 West Taylor Street, Chicago, Illinois 60612, United States

Abstract. Intrinsic optical signal (IOS) imaging promises a noninvasive method for advanced study and diagnosis of eye diseases. Before pursuing clinical applications, it is essential to understand anatomic and physiological sources of retinal IOSs and to establish the relationship between IOS distortions and eye diseases. The purpose of this study was designed to demonstrate the feasibility of *in vivo* IOS imaging of mouse models. A high spatiotemporal resolution spectral domain optical coherence tomography (SD-OCT) was employed for depth-resolved retinal imaging. A custom-designed animal holder equipped with ear bar and bite bar was used to minimize eye movements. Dynamic OCT imaging revealed rapid IOS from the photoreceptor's outer segment immediately after the stimulation delivery, and slow IOS changes were observed from inner retinal layers. Comparative photoreceptor IOS and electroretinography recordings suggested that the fast photoreceptor IOS may be attributed to the early stage of phototransduction before the hyperpolarization of retinal photoreceptor. © *2016 Society of Photo-Optical Instrumentation Engineers (SPIE)* [DOI: 10.1117/1.JBO.21.9.096010]

Keywords: Intrinsic optical signal; functional imaging; optical coherence tomography; physiology; retina; eye.

Paper 160376PR received Jun. 16, 2016; accepted for publication Aug. 26, 2016; published online Sep. 21, 2016.

1 Introduction

Eye diseases, such as age-related macular degeneration (AMD),[1] retinitis pigmentosa (RP),[2] diabetic retinopathy,[3,4] and glaucoma[5,6] can produce retinal neural dysfunctions that lead to severe vision loss if appropriate interventions are not involved promptly. It is known that different eye diseases damage different retinal cells, which are located in different functional layers. For example, retinal photoreceptors are vulnerable in AMD[1] and ganglion cells are affected in glaucoma.[6] Electroretinography (ERG)[7] and multifocal ERG[8,9] can provide objective evaluation of retinal neural dysfunction, but the spatial resolution is limited due to the integral effect of bioelectric signals from multiple retinal layers. Each hexagonal stimulus pattern used in multifocal ERG usually has an angular size of ~5 deg,[8,9] corresponding to ~2-mm resolution in the human retina. Therefore, accurate separation of ERG components of retinal neurons is difficult. The low signal selectivity of ERG due to the integral effect makes its interpretation complicated for clinical diagnoses. Optical methods, such as fundus photography and optical coherence tomography (OCT),[10] can provide high-resolution examination of retinal morphology. However, morphological images do not directly provide functional information of retinal physiology. A high-resolution method for objective evaluation of retinal physiological function is desirable for early disease detection and improved treatment evaluation.

Intrinsic optical signal (IOS) imaging has promise as a high-resolution method for objective assessment of retinal neural dysfunctions due to eye diseases.[11] Micrometer level (<3 μm) resolution has been achieved for *in vivo* IOS imaging of frog retinas using custom-designed confocal[12] and OCT[13] systems. Stimulus-evoked IOSs have been observed in multiple animal models[12–28] and human subjects.[29] Recent OCT studies revealed rapid IOS changes at photoreceptor outer segments.[13,28] *In vitro* IOS imaging of normal and mutant mouse retinas has been conducted to demonstrate disease-produced IOS distortions.[30] Laser-injured frog eyes have been used to demonstrate *in vivo* IOS mapping of localized retinal dysfunction.[27] Both *in vitro* and *in vivo* studies have shown that fast IOSs have different polarities and mainly originate from the photoreceptor outer segments in frog retinas.[11] These studies also revealed that photoreceptor IOSs had a rapid time course (<4 ms after onset of the light stimulus).[13,28] Transient retinal phototropism was reported to be one factor that generates photoreceptor IOSs,[31–33] but the IOS physiological source has not been accurately determined yet. Before pursuing clinical applications, it is necessary to establish the relationship between IOS distortions and eye diseases. Multiple mouse models are available to characterize IOS abnormalities in diseased retinas. However, *in vivo* IOS imaging of mouse retinas is technically difficult due to small ocular lens and inevitable eye movements.

The purpose of this study was designed to demonstrate the feasibility of *in vivo* IOS imaging of mouse models. Some part of the results has been reported in the SPIE Proceedings.[34] To achieve high spatiotemporal resolution imaging, a high-speed [up to 1250 frames per second (fps)] and high-resolution (~3 μm in both lateral and axial directions) spectral domain OCT (SD-OCT) was constructed. Comparative IOS and ERG measurements were conducted to investigate the physiological mechanism of retinal IOSs.

---

*Address all correspondence to: Xincheng Yao, E-mail: xcy@uic.edu

2 Methods

2.1 Experimental Setup

Figure 1(a) shows a schematic diagram of our custom-designed SD-OCT. A wide bandwidth near-infrared (NIR; $\Delta\lambda = 100$ nm, $\lambda = 850$ nm) superluminescent diode (SLD; D-840-HP-I, Superlum) was used as the OCT light source to provide high axial resolution (~ 3 μm). The NIR light was focused on the retina through optical lenses and the mouse eye and was scanned with a galvo mirror (GVS001, Thorlabs, Inc.) to produce OCT B-scan images. The pivot of the galvo mirror was conjugate to the pupil of the mouse eye to minimize the vignetting effect. The lateral resolution of the system was about 3 μm. A green ($\lambda = 505$ nm) light-emitting diode (LED; M505L3, Thorlabs, Inc.) was coupled into the imaging system with a dichroic mirror (DMLP650R, Thorlabs, Inc.) for retinal stimulation. For easy alignment of the mouse eye, a pupil camera was integrated into the system. A custom-designed spectrometer was constructed for OCT recording. The linear camera (EV71YEM4CL2014-BA9, e2v) used in the OCT provided a line rate up to 70,000 lines/s. The high-imaging speed minimized the in-frame image blur and between-frame displacement and, thus, reduced the effect of eye movements to enable robust observation of transient IOS responses correlated with retinal stimulation.

Figure 1(b) shows a photograph of our custom-designed animal holder. Since IOSs measure pixel intensity changes in captured images, the IOS imaging quality is extremely sensitive to movements. Eye movements caused by the breath and heart-beats can be significant if the mouse head is not appropriately fixated. The combined bite bar and ear bar system has been used in stereotaxic surgeries.[35,36] However, commercial stereotaxic frames cannot be directly used for mouse imaging because they do not provide enough degrees of freedom to align the mouse eye for OCT recording. To achieve a robust IOS recording, we designed an animal holder with five degrees of freedom (i.e., x, y, z, pitch, and roll) and integrated the bite bar and ear bar system. Two linear translation stages and one mini lab jack were used to provide x, y, and z alignments, a θ translation stage was used for pitch alignment, and a cassette was used to provide roll adjustment of the imaged mouse. The bite bar and ear bar system was fixed at the end of the cassette.

2.2 Animal Preparation

Adult (3 to 6 months old) wild-type mice (strain C57BL/6J, The Jackson Laboratory) were used in this study. Before the experiment, each mouse was first dark or light adapted (~ 500 cd/m^2) for 3 h, and then was anesthetized with 60 mg/kg ketamine and 3 mg/kg xylazine given by intraperitoneal injection. After the mouse was fully anesthetized, it was transferred to the custom-designed animal holder with the head fixed by an ear bar and bite bar. A drop of 1% atropine was applied to the mouse eye for pupil dilation. An ERG active electrode was placed in contact with the cornea. One drop of ophthalmic gel was applied to each eye to keep them from clouding. A cover glass was placed on the imaged eye ball. The cover glass along with the gel worked as a contact lens to improve image resolution by reducing optical aberrations of the mouse eye.[37] During the recording, a heating pad was wrapped around the animal holder to keep the mouse warm. All experiments were performed following the protocols approved by the Animal Care Committee at the University of Illinois at Chicago.

2.3 Data Acquisition

For IOS measurement, OCT images in Fig. 3 were recorded at 200 fps. After a 1-s prestimulus recording, a 10-ms light flash, with different intensities varying 20 dB (-20, -16, -13, -9.5, -6.3, -2.6, and 0 dB relative to maximum intensity, where the maximum intensity of 0 dB was measured 2×10^7 photons · μm^{-2}· ms^{-1} on cover glass) was introduced for retinal stimulation. After the onset of the stimulus, OCT images were recorded for 4 s. For high-speed IOS recording (Fig. 6), the line number in OCT B-scans was reduced so that recording speed increased to 1250 fps. A -9.5-dB 10-ms flash was introduced after an 80-ms prestimulus recording. IOSs were recorded for 160 ms after onset of the stimulus. All data were saved to a computer hard drive for post processing. Although a head fixation method was used, there was still detectable bulk motion in the OCT images. Residual bulk motion was digitally compensated for by accurate image registration using an algorithm described in a previous publication.[13] Subsequently, the OCT images were then used for calculating IOSs using a custom developed MATLAB® (MathWorks, Natick, Massachusetts) program. The data processing procedure has been described previously.[38]
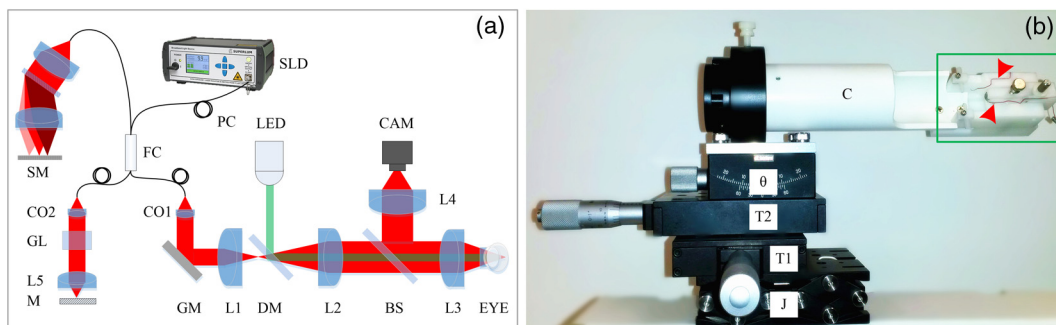
Fig. 1 (a) Schematic diagram of the custom-designed OCT used for *in vivo* IOS imaging of mouse retinas. SLD: superluminescent diode; SM: spectrometer; PC: polarization controller; FC: 90:10 fiber coupler; CAM: camera; LED: light-emitting diode; CO1–CO2: collimators; L1–L5: lenses; GL: glass blocks; M: mirror; GM: galvo mirror; DM: dichroic mirror; BS: beam splitter. (b) Photograph of the custom-designed animal holder. J is a mini lab jack for *z* adjustment, T1 and T2 are translational stages for *x* and *y* adjustments, θ is the θ translation stage for pitch adjustment, C is the mouse cassette where the mouse was placed. The green rectangle shows the bite bar and ear bar unit. The red arrowheads indicate the ERG electrodes.

For ERG recording, a silver electrode with the tip bent to a ring was placed in contact with the mouse cornea and served as an active electrode; a silver reference electrode was twisted on the bite bar so that it contacted the mouse mouth reliably when the head was fixed. ERG recordings were amplified 1000 times and filtered (pass band: 1 to 1000 Hz) by a differential amplifier (DAM50, World Precision Instruments). The amplified and filtered ERG recordings were then sampled by a data acquisition board (PCIe-6351, National Instruments) at 40,000 samples/s and saved to a computer hard drive.

3 Results

Figure 2 shows a single frame and the average of 10 OCT B-scan images with a frame resolution of 600 pixels × 230 pixels. Figure 2(a) shows a representative B-scan around the optic nerve head. Figure 2(b) shows a B-scan ~0.6 mm away from the optic nerve head where individual retinal layers, including the inner plexiform layer (IPL), inner nuclear layer (INL), outer plexiform layer (OPL), outer nuclear layer (ONL), external limiting membrane (ELM), inner segment ellipsoid (ISe), outer segment (OS), retinal pigment epithelium (RPE) and choroid, were clearly observed. Averaged B-scans in Figs. 2(a2) and 2(b2) show a clearer layered structure due to an increased signal to noise ratio (SNR).

Figure 3 shows representative IOS results from different stimulation and light adaptation conditions. In dark adapted retinas, robust rapid IOSs were observed from photoreceptor outer segments immediately after stimulation delivery [Figs. 3(a) and 3(b)]. Unambiguous IOS changes, with a delayed time course, were also observed from the IPL in the retina with 500-ms stimulation [Figs. 3(b5) and 3(b6)]; while no reliable IOSs from the IPL were observed in the retina with 10-ms stimulation. The yellow curve in Fig. 3(b1) shows more activated pixels at 0.5 s in outer retinal layers under 500-ms stimulation than those in Fig. 3(a1) under 10-ms stimulation. When the retina was light adapted and rods were bleached, no IOS response was observable from the IOS images [Figs. 3(c2)–3(c6)]. We plotted IOS curves from different layers, as shown in Fig. 3(d). The curves were calculated by averaging pixel intensities of all active pixels in corresponding layers [shown as green and red pixels in

Figs. 3(a1), 3(b1), and 3(c1)]. The curves were then normalized by multiplying the active pixel ratio in corresponding retinal layers. Robust rapid IOSs were observed from ISe, OS, and RPE layers in dark adapted retinas [Figs. 3(d1) and 3(d2)] immediately after stimulus onset [Figs. 3(e1) and 3(e2)]. When the retina was stimulated with 500-ms light, robust slow IOSs were observed from the IPL [Fig. 3(d2)]. The IOS onset time from the IPL was ~0.5 s. In the light-adapted retina, IOSs of all retinal layers were hardly observable and magnitudes were relatively small, compared to those in dark adapted retinas. Figure 3(e3) revealed low magnitude, rapid IOS changes (arrowheads) immediately after stimulation delivery from the OS and RPE layers. *In vivo* mouse IOS properties were similar to those we observed in frogs.[13] IOSs from outer retinal layers shown in Fig. 3(e3) suffered from high noise level. To confirm the IOSs in light condition, an additional seven experiments were conducted with light-adapted retinas. Figure 4 illustrates average IOS changes of eight retinas, and convincible IOS was observed from the outer retina (i.e., ISe, OS, and RPE) immediately after the stimulation delivery.

Photoreceptor IOS and ERG a-wave responses to different stimulation conditions were recorded to investigate the IOS physiological origin in mice. The retinas were stimulated by 10-ms light flashes with intensities varying 20 dB. Three trials were conducted for each stimulation intensity. Figure 5(a) shows averaged photoreceptor IOS curves and Fig. 5(b) shows representative single trial ERG curves at different stimulation intensities. It was observed that the amplitude and time scales of photoreceptor IOS and ERG a-wave were both dependent on the stimulation intensity. The dependency was shown more clearly in the enlarged view in Fig. 5(c). Figure 5(c) also showed that photoreceptor IOSs appeared earlier than ERG a-waves under the same stimulation intensity. From Fig. 5(d), we can see that photoreceptor IOS and ERG a-wave amplitudes changed very similarly; i.e., both increased as stimulation intensity increased and reached a peak at −2.6-dB stimulus intensity. As photoreceptor IOS amplitudes increased, the IOS SNR also increased and reached a peak at −6.3-dB stimulation intensity [Fig. 5(f)]. Photoreceptor IOS and ERG a-wave time-to-half-peak (time for IOS or ERG a-wave to reach half maximum)
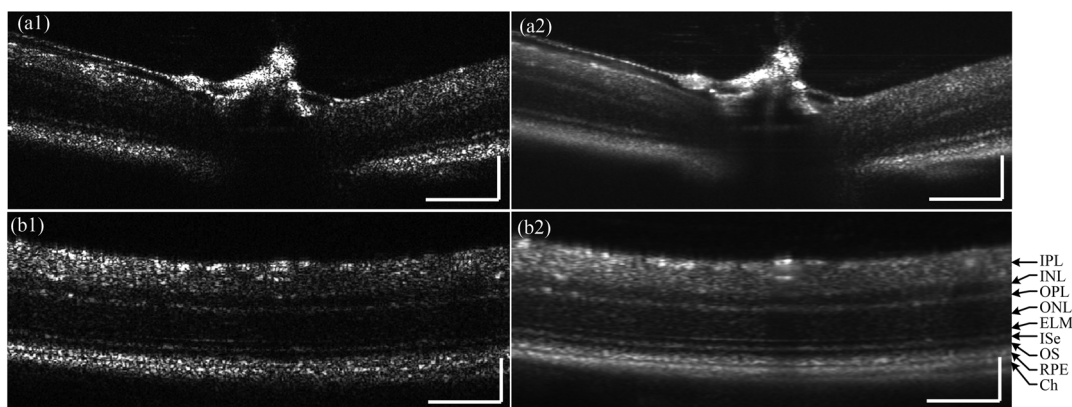
Fig. 2 Mouse retinal B-scans acquired with the custom built SD-OCT. (a1) Single frame retinal B-scan of the optic nerve head, and (a2) average of 10 frames. (b1) Single frame retinal B-scan ~0.6 mm away from the optic nerve head, and (b2) average of 10 frames showing clear retinal layers including the: IPL: inner plexiform layer, INL: inner nuclear layer, OPL: outer plexiform layer, ONL: outer nuclear layer, ELM: external limiting membrane, ISe: inner segment ellipsoid, OS: outer segment, RPE: retinal pigment epithelium, and Ch: choroid. Scale bars: 100 μm.
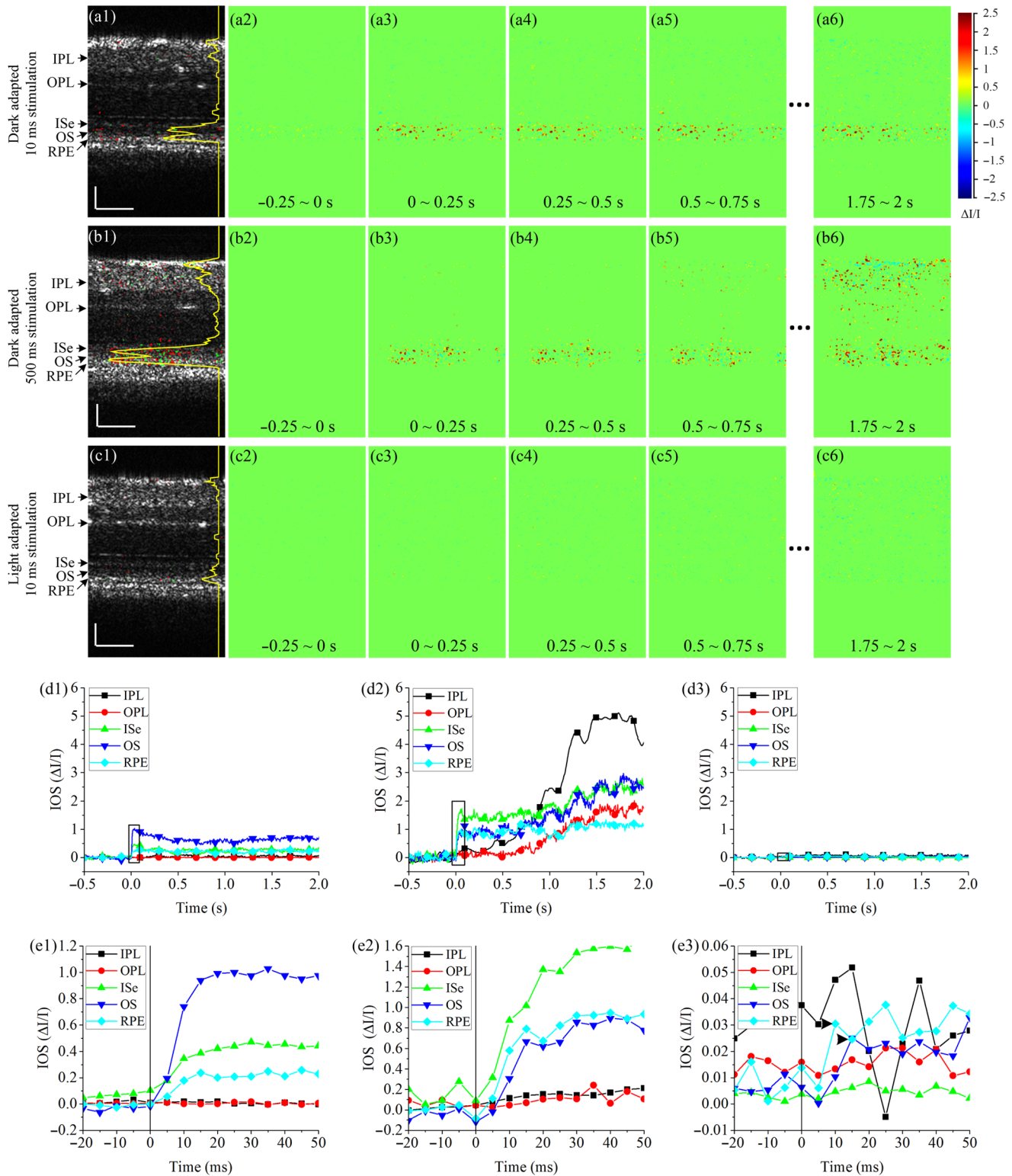
Fig. 3 Representative *in vivo* IOS imaging results under different stimulation and light adaptation conditions. Stimulation intensity was −9.5 dB. (a) IOS imaging results from dark adapted retina with 10-ms light stimulation. (a1) Activated pixels at 0.5 s. The yellow curve shows the active pixel number. (a2)–(a6) IOS images at different times. (b) IOS imaging results from dark adapted retina with 500-ms light stimulation. (b1) Activated pixels at 0.5 s. The yellow curve shows the active pixel number. (b2)–(b6) IOS images at different times. (c) IOS imaging results from light-adapted retina with 10-ms light stimulation. (c1) activated pixels at 0.5 s. The yellow curve shows the active pixel number. (c2)–(c6) IOS images at different times. (d) Absolute IOS curves from different retinal layers calculated from experimental trials corresponding to panels (a), (b), and (c). IOS curves were normalized by multiplying the active pixel ratio in corresponding retinal layers. (e) Enlarged views of black rectangle areas in (d). (e1)–(e3) correspond to (d1)–(d3), respectively. Vertical lines show stimulus onset. Arrowheads in (e3) indicate IOS peaks. Scale bars in (a), (b), and (c): 50 μm.
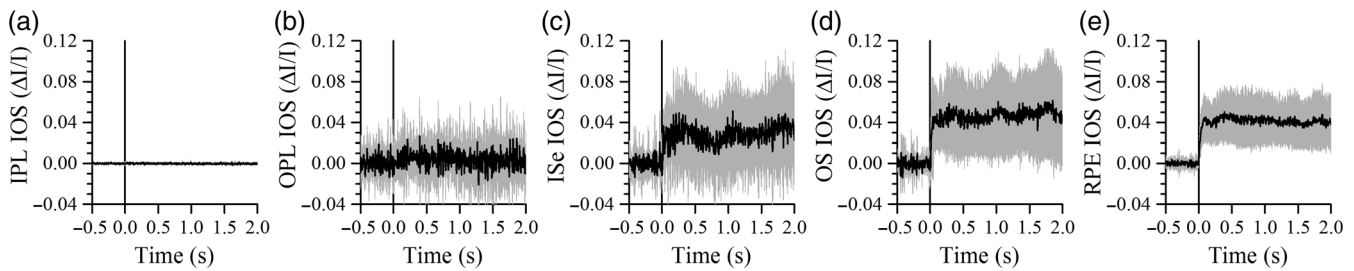
Fig. 4 Averaged IOSs of (a) IPL, (b) OPL, (c) ISe, (d) OS, and (e) RPE layers in light-adapted retinas. Each curve is average of eight experimental trials. Gray areas show standard deviation. Vertical lines show stimulus onset.

responded similarly to stimulation intensity, i.e., both decreased as stimulation intensity increased [Fig. 5(e)].

To further understand the physiological source of photoreceptor IOS, we increased IOS imaging speed to detect the photoreceptor IOS and ERG a-wave onset times in dark adapted retinas. The onset time was defined as the time for photoreceptor IOS or ERG a-wave to reach the amplitude of 3σ, where σ was the standard deviation of the prestimulus IOS/ERG amplitude. Linear interpolation was used if 3σ fell between the observed data points. We chose a moderate stimulation intensity of −9.5 dB, which corresponded to the fourth data point in Figs. 5(d)–5(f). To increase IOS imaging speed, we decreased the A-line number and increased the IOS imaging speed from 200 to 1250 fps; the corresponding time resolution was increased from 5 to 0.8 ms. Figure 6(a) shows the IOS map and IOS images acquired at 1250 fps. Three photoreceptor IOS and ERG curves recorded from different retinas were plotted together for comparison in Fig. 6(b). It was clearly observed

that photoreceptor IOS onset time was shorter than ERG a-wave onset time. Onset time of each curve in Fig. 6(b) was calculated and then averaged for quantitative comparison in Fig. 6(c). We can see that the photoreceptor IOS onset time was 1.1 ± 0.2 ms, while the ERG a-wave onset time was 5.0 ± 0.5 ms.[39] The difference was statistically significant with a *p*-value smaller than 0.001 using a single sided *t*-test. Figure 6(d) shows the averaged photoreceptor IOS and ERG curves. The vertical dashed lines show onset times calculated based on the averaged curves. As a result of averaging, noise level was reduced, thus the 3σ was reduced, resulting in smaller calculated onset times. It is shown that the photoreceptor IOS onset time was as short as ∼0.4 ms while ERG onset time was ∼3.9 ms.

4 Discussion

In summary, the feasibility of *in vivo* IOS imaging of mouse models was demonstrated using a custom-designed functional
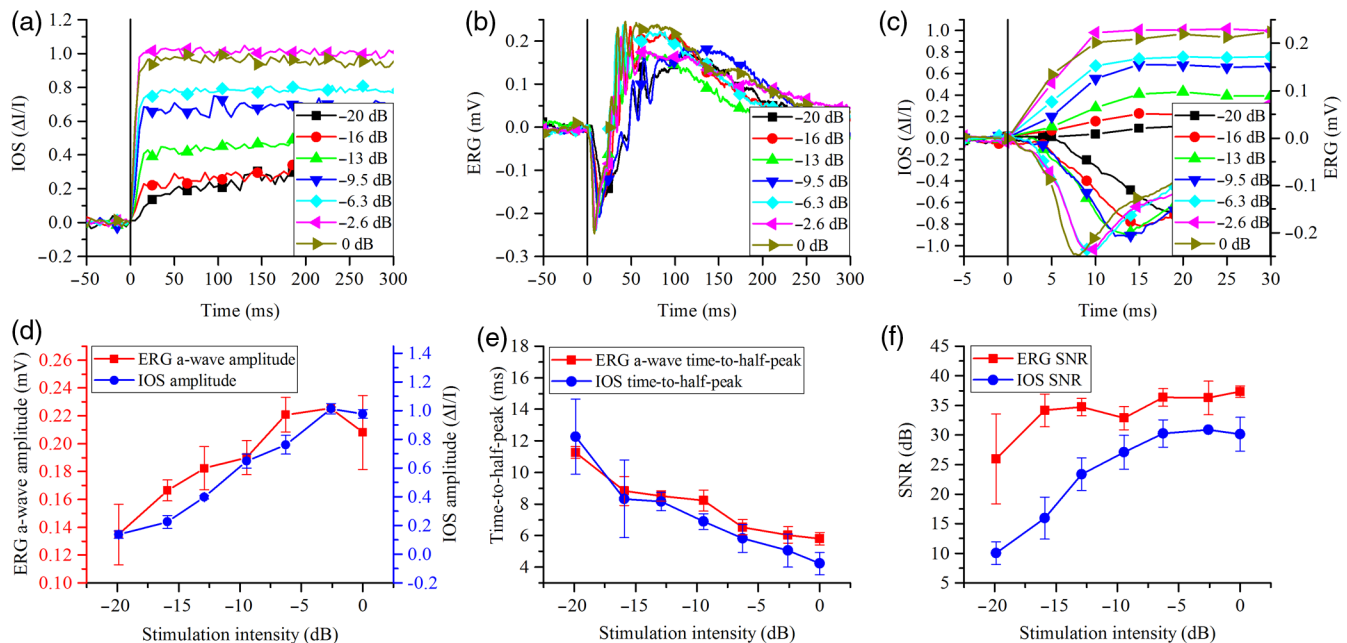
Fig. 5 Photoreceptor IOS and ERG responses under different stimulation intensities. (a) Absolute photoreceptor IOS curves under different stimulation intensities. Vertical line shows stimulus onset. Each curve represents an average of three experimental trials. (b) Representative ERGs under different stimulation intensities. Vertical line shows stimulus onset. (c) Photoreceptor IOSs (curves above $y = 0$) and ERGs (curves below $y = 0$) from −5 to 30 ms. Vertical line shows stimulus onset. (d) ERG a-wave and photoreceptor IOS amplitude changes as a function of stimulation intensity. (e) ERG a-wave and photoreceptor IOS time-to-half-peak changes as a function of stimulation intensity. (f) Photoreceptor IOS and ERG SNR changes as a function of stimulation intensity.
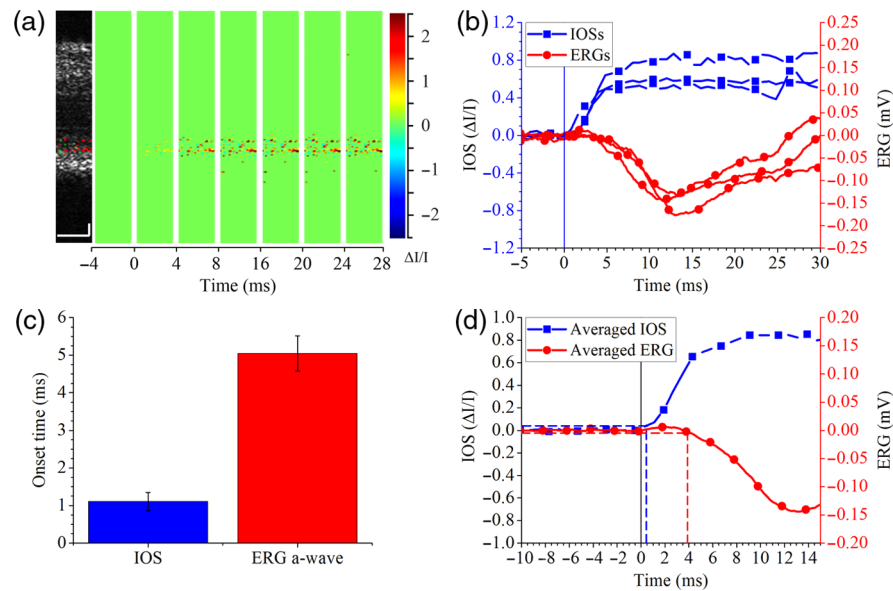
Fig. 6 (a) IOS imaging with 1250 fps OCT. (b) Photoreceptor IOS and ERG changes. IOSs and ERGs were recorded from three different retinas. Vertical line shows stimulus onset. (c) Comparison between average photoreceptor IOS and ERG a-wave onset times. (d) Averaged photoreceptor IOS and ERG corresponding to the IOS and ERG curves in (b). Vertical solid line shows stimulus onset. Horizontal dashed lines show 3σ of prestimulus IOS (blue) and ERG (red) amplitudes. Vertical dashed lines show IOS (blue) and ERG (red) onset times. Scale bars in A: 25 μm.

OCT. We were aware of that head restraining devices; i.e., bite bar and ear bar, were essential for reducing eye movement to improve IOS quality. Photoreceptor IOS and ERG a-wave magnitude showed a similar response to variable stimulation intensity (Figs. 5(d)–5(e)]. High-speed (1250 fps) IOS imaging revealed that the photoreceptor IOS onset time was ~1.1 ms, while the ERG a-wave onset time was ~5.0 ms at stimulation intensity of −9.5 dB.

Figures 3(d1) and 3(d2) show similar IOSs from RPE, OS and ISe layers in dark adapted retinas. We speculated that the RPE IOS were contributed by photoreceptor OSs because the OSs can penetrate into the RPE layer.[40] ISe IOS may also come from OSs because the ISe and OSs are immediately adjacent and the active pixels were mainly at the outer part of the ISe [yellow curves in Figs. 3(a1) and 3(b1)], which could actually be the OS because OCT axial resolution (~3 μm) was not high enough to differentiate those layers.[41] Thus fast IOS observed was mainly from photoreceptor OS.[13] It is well established that ERG a-wave is the result of the phototransduction process in photoreceptor OS. It reflects the closure of cyclic guanosine monophosphate gated channels on photoreceptor membrane and dark current reduction due to light absorption in OS.[42,43] Considering that both photoreceptor IOS and ERG a-wave are from OS and that photoreceptor IOS and ERG a-wave were closely correlated [Figs. 5(d)–5(e)], we speculate that the rapid photoreceptor IOS also originated from phototransduction processes.

From Fig. 5(c) we could see that photoreceptor IOS onset times were shorter than ERG a-wave onset times. High-speed OCT showed that photoreceptor IOS onset time was ~3.9 ms shorter [Fig. 6(b) and 6(c)] under −9.5 dB stimulation intensity. Since photoreceptor IOS onset time was shorter than ERG a-wave onset time, it suggests that the photoreceptor originated from the early stage of phototransduction before the hyperpolarization of the retinal photoreceptor, which generates ERG

a-wave. According to Yoshizawa and Kandori,[44] the time required for rhodopsin to absorb photons and become enzymatically active is around 1 ms. Figure 6(d) shows that, when averaged, photoreceptor IOS could be observed at ~0.4 ms, and this confirmed that photoreceptor IOS originated from early phototransduction.

Rapid IOSs were observed in light-adapted retinas from outer retinal layers [Figs. 3(d3) and 4(c)–4(e)]. Such signals possibly originated from cones in light-adapted retinas. Given the fact that cones only account for ~3% of all photoreceptors in mice, the total IOS in light-adapted retinas should be small, compared to that in dark adapted retinas. In animal models with more cones, e.g., frogs where cone ratio is ~50%, larger light-adapted IOS was observed.[13] The resolution of our current system is not high enough to directly differentiate mouse rods and cones (rod OS diameter ~1.4 μm, cone OS diameter ~1.2 μm[45]). Further investigation with adaptive optics OCT may enable further verification of the anatomic origination of the IOS changes.

In the retinas with prolonged stimulation, slow IOS was observed from inner retinal layers [Figs. 3(b) and 3(d2)]. We speculate that the slow IOS may involve the complications of nonlinear information processing in the retina as well as retina adaptation to stimulation. Light-induced hemodynamic change may also partially contribute to the slow IOS.[46] Further investigation is required to understand the origination of slow IOS.

Further *in vivo* and *in vitro* studies that use transgenic mouse models or use pharmacological agents to block specific phototransduction processes could help accurately identify photoreceptor IOS origination, and thus provide a method for advanced study and diagnosis of retinal diseases that cause photoreceptor dysfunction, such as AMD and RP. There are no readily available medicines or surgical procedures that could reverse photoreceptor degeneration and totally restore its function. The key to prevent vision loss is to diagnose retinal

diseases in the early stages and apply intervention properly. By providing unparalleled spatial resolution and signal selectivity, we anticipate that further development of functional OCT of retinal IOSs will pave the way for early detection of retinal diseases and objective evaluation of clinical treatments.

5 Conclusion

This study demonstrates the feasibility of *in vivo* IOS imaging of mouse models using a custom-designed functional OCT. Comparative IOS imaging and ERG measurements suggest that the fast photoreceptor IOS may be attributed to the early stage of phototransduction before the hyperpolarization of the retinal photoreceptor. Further development of the functional OCT for *in vivo* IOS imaging of retinal photoreceptors may lead to a feasible method for objective assessment of retinal photoreceptor dysfunctions due to eye diseases.

References

1. C. A. Curcio, N. E. Medeiros, and C. L. Millican, "Photoreceptor loss in age-related macular degeneration," *Invest. Ophthalmol. Vis. Sci.* **37**(7), 1236–1249 (1996).
2. D. Nagy et al., "Long-term follow-up of retinitis pigmentosa patients with multifocal electroretinography," *Invest. Ophthalmol. Vis. Sci.* **49**(10), 4664–4671 (2008).
3. Y. Qin, G. Xu, and W. Wang, "Dendritic abnormalities in retinal ganglion cells of three-month diabetic rats," *Curr. Eye Res.* **31**(11), 967–974 (2006).
4. B. Meyer-Rusenberg et al., "Pathological changes in human retinal ganglion cells associated with diabetic and hypertensive retinopathy," *Graefes Arch. Clin. Exp. Ophthalmol.* **245**(7), 1009–1018 (2007).
5. R. S. Harwerth and H. A. Quigley, "Visual field defects and retinal ganglion cell losses in patients with glaucoma," *Arch. Ophthalmol.* **124**(6), 853–859 (2006).
6. R. W. Nickells, "Ganglion cell death in glaucoma: from mice to men," *Vet. Ophthalmol.* **10**(Suppl 1), 88–94 (2007).
7. H. P. Scholl and E. Zrenner, "Electrophysiology in the investigation of acquired retinal disorders," *Surv. Ophthalmol.* **45**(1), 29–47 (2000).
8. S. L. Ball and H. M. Petry, "Noninvasive assessment of retinal function in rats using multifocal electroretinography," *Invest. Ophthalmol. Vis. Sci.* **41**(2), 610–617 (2000).
9. D. C. Hood, "Assessing retinal function with the multifocal technique," *Prog. Retin. Eye Res.* **19**(5), 607–646 (2000).
10. C. A. Puliafito et al., "Imaging of macular diseases with optical coherence tomography," *Ophthalmology* **102**(2), 217–229 (1995).
11. X. Yao and B. Wang, "Intrinsic optical signal imaging of retinal physiology: a review," *J. Biomed. Opt.* **20**(9), 090901 (2015).
12. Q. X. Zhang et al., "In vivo confocal imaging of fast intrinsic optical signals correlated with frog retinal activation," *Opt. Lett.* **36**(23), 4692–4694 (2011).
13. Q. Zhang et al., "Functional optical coherence tomography enables in vivo physiological assessment of retinal rod and cone photoreceptors," *Sci. Rep.* **5**, 9595 (2015).
14. K. Bizheva et al., "Optophysiology: depth-resolved probing of retinal physiology with functional ultrahigh-resolution optical coherence tomography," *Proc. Natl. Acad. Sci. U. S. A.* **103**(13), 5066–5071 (2006).
15. V. J. Srinivasan et al., "In vivo measurement of retinal physiology with high-speed ultrahigh-resolution optical coherence tomography," *Opt. Lett.* **31**(15), 2308–2310 (2006).
16. X. C. Yao and J. S. George, "Near-infrared imaging of fast intrinsic optical responses in visible light-activated amphibian retina," *J. Biomed. Opt.* **11**(6), 064030 (2006).
17. G. Hanazono et al., "Intrinsic signal imaging in macaque retina reveals different types of flash-induced light reflectance changes of different origins," *Invest. Ophthalmol. Vis. Sci.* **48**(6), 2903–2912 (2007).
18. D. Ts'o et al., "Noninvasive functional imaging of the retina reveals outer retinal and hemodynamic intrinsic optical signal origins," *Jpn. J. Ophthalmol.* **53**(4), 334–344 (2009).
19. X. C. Yao, "Intrinsic optical signal imaging of retinal activation," *Jpn. J. Ophthalmol.* **53**(4), 327–333 (2009).
20. Y. C. Li et al., "Parallel optical monitoring of visual signal propagation from the photoreceptors to the inner retina layers," *Opt. Lett.* **35**(11), 1810–1812 (2010).
21. Y. G. Li et al., "High-speed line-scan confocal imaging of stimulus-evoked intrinsic optical signals in the retina," *Opt. Lett.* **35**(3), 426–428 (2010).
22. Y. G. Li et al., "High spatiotemporal resolution imaging of fast intrinsic optical signals activated by retinal flicker stimulation," *Opt. Express* **18**(7), 7210–7218 (2010).
23. Q. X. Zhang et al., "Microlens array recording of localized retinal responses," *Opt. Lett.* **35**(22), 3838–3840 (2010).
24. A. A. Moayed et al., "In vivo imaging of intrinsic optical signals in chicken retina with functional optical coherence tomography," *Opt. Lett.* **36**(23), 4575–4577 (2011).
25. A. Akhlagh Moayed et al., "Correlation of visually evoked intrinsic optical signals and electroretinograms recorded from chicken retina with a combined functional optical coherence tomography and electroretinography system," *J. Biomed. Opt.* **17**(1), 016011 (2012).
26. X. C. Yao and Y. C. Li, "Functional imaging of retinal photoreceptors and inner neurons using stimulus-evoked intrinsic optical signals," *Methods Mol. Biol.* **884**, 277–285 (2013).
27. Q. X. Zhang et al., "In vivo confocal intrinsic optical signal identification of localized retinal dysfunction," *Invest. Ophthalmol. Vis. Sci.* **53**(13), 8139–8145 (2012).
28. B. Wang et al., "En face optical coherence tomography of transient light response at photoreceptor outer segments in living frog eyecup," *Opt. Lett.* **38**(22), 4526–4529 (2013).
29. V. J. Srinivasan et al., "In vivo functional imaging of intrinsic scattering changes in the human retina with high-speed ultrahigh resolution OCT," *Opt. Express* **17**(5), 3861–3877 (2009).
30. Q. X. Zhang et al., "Comparative intrinsic optical signal imaging of wild-type and mutant mouse retinas," *Opt. Express* **20**(7), 7646–7654 (2012).
31. R. Lu et al., "Dynamic near-infrared imaging reveals transient phototropic change in retinal rod photoreceptors," *J. Biomed. Opt.* **18**(10), 106013 (2013).
32. B. Wang et al., "Functional optical coherence tomography reveals transient phototropic change of photoreceptor outer segments," *Opt. Lett.* **39**(24), 6923–6926 (2014).
33. X. Zhao et al., "Stimulus-evoked outer segment changes in rod photoreceptors," *J. Biomed. Opt.* **21**(6), 065006 (2016).
34. B. Wang and X. Yao, "In vivo intrinsic optical signal imaging of mouse retinas," *Proc. SPIE* **9693**, 96930H (2016).
35. G. Paxinos et al., "Bregma, lambda and the interaural midpoint in stereotaxic surgery with rats of different sex, strain and weight," *J. Neurosci. Methods* **13**(2), 139–143 (1985).
36. B. M. Geiger et al., "Survivable stereotaxic surgery in rodents," *J. Vis. Exp.* **2008**(20).
37. X. Liu et al., "Effect of contact lens on optical coherence tomography imaging of rodent retina," *Curr. Eye Res.* **38**(12), 1235–1240 (2013).
38. X. C. Yao and Y. B. Zhao, "Optical dissection of stimulus-evoked retinal activation," *Opt. Express* **16**(17), 12446–12459 (2008).
39. D. I. Hamasaki et al., "The a-wave latency in control subjects and patients with retinal diseases," *Jpn. J. Ophthalmol.* **46**(4), 433–442 (2002).
40. O. Strauss, "The retinal pigment epithelium in visual function," *Physiol. Rev.* **85**(3), 845–881 (2005).
41. R. W. Lu et al., "Investigation of the hyper-reflective inner/outer segment band in optical coherence tomography of living frog retina," *J. Biomed. Opt.* **17**(6), 060504 (2012).
42. R. D. Penn and W. A. Hagins, "Signal transmission along retinal rods and the origin of the electroretinographic a-wave," *Nature* **223**(5202), 201–205 (1969).

43. A. J. Sillman, H. Ito, and T. Tomita, "Studies on the mass receptor potential of the isolated frog retina II. On the basis of the ionic mechanism," *Vision Res.* **9**(12), 1443–1451 (1969).
44. T. Yoshizawa and H. Kandori, "Primary photochemical events in the rhodopsin molecule," *Progr. Retinal Res.* **11**, 33-55 (1991).
45. Y. Fu and K. W. Yau, "Phototransduction in mouse rods and cones," *Pflugers Arch.* **454**(5), 805–819 (2007).
46. T. Son et al., "Optical coherence tomography angiography of stimulus evoked hemodynamic responses in individual retinal layers," *Biomed. Opt. Express* **7**(8), 3151–3162 (2016).

Benquan Wang received his bachelor's degree in biomedical engineering from Tianjin University in 2012. He is a PhD candidate in the Department of Bioengineering, University of Illinois at Chicago. His research interests include biomedical optics and retinal study.

Yiming Lu received his bachelor's and master's degrees in biomedical engineering from Tianjin University in 2011 and 2014, respectively. He is a PhD student in the Department of Bioengineering, University of Illinois at Chicago. His research interests include biomedical optics and retinal study.

Xincheng Yao received his PhD in optics from the Institute of Physics, Chinese Academy of Sciences, in 2001. He is a professor in the Department of Bioengineering, University of Illinois at Chicago. His research interests include biomedical optics instrumentation and retinal imaging.